PAPER

Check for updates

A cascaded SrTiO$_3$/TiO$_2$/SrTiS$_3$ heterojunction with enhanced charge separation for highly efficient photocatalytic hydrogen production

Chan Lu,[a] Xiaolong Li,[b] Yongning Ma [ID][b] and Yuhao Yang [ID] *[b]

Designing efficient catalysts for photocatalytic hydrogen production is a significant challenge due to the intrinsic limitations of wide-band-gap semiconductors, such as severe charge recombination and poor visible-light absorption. Herein, a novel SrTiO$_3$/TiO$_2$/SrTiS$_3$ ternary heterojunction is rationally designed and fabricated *via* a controllable, one-step thermal vulcanization strategy to overcome these limitations. Structural and morphological characterization confirms the successful formation of an intimate three-component heterostructure. The resulting composite exhibits a significantly broadened light absorption range extending into the visible region. More importantly, photoelectrochemical measurements reveal that the ternary heterojunction possesses vastly superior charge separation and transfer efficiency compared to its individual counterparts. Consequently, the optimized photocatalyst demonstrates a remarkable, over 11-fold enhancement in H$_2$ evolution activity compared to pristine SrTiO$_3$, and maintains excellent stability in cycling tests. The outstanding performance is attributed to a multi-step charge separation mechanism across the dual type-II interfaces. This unique architecture synergistically combines the enhanced light harvesting of the SrTiS$_3$ sensitizer with the efficient spatial separation of photogenerated electrons and holes. This work provides a robust strategy for designing advanced multi-component sulfide/oxide heterojunctions for efficient solar energy conversion.

1 Introduction

The escalating global demand for energy, met predominantly by finite fossil fuels, has created profound environmental and geopolitical challenges. The combustion of these resources is the primary source of anthropogenic greenhouse gases, such as carbon dioxide (CO$_2$), which drive climate change manifested by global warming, extreme weather phenomena, and rising sea levels.[1] This critical situation necessitates a comprehensive transition to cleaner and more sustainable energy systems to mitigate environmental degradation and ensure long-term energy security.[2] Among various alternative energy carriers, hydrogen (H$_2$) has emerged as a particularly promising candidate. It is distinguished by its high gravimetric energy density (142 MJ kg^{-1}) and its potential for carbon-neutral utilization, as its combustion or electrochemical conversion in fuel cells yields only water (H$_2$O).[3,4] Consequently, a "hydrogen economy" is envisioned as a cornerstone of a future sustainable energy landscape, contingent upon the development of efficient and cost-effective methods for producing H$_2$ from renewable sources.

Photocatalytic hydrogen evolution from water represents a highly promising and sustainable pathway for producing this clean chemical fuel.[5,6] This process harnesses solar energy to drive the reduction of protons (H$^+$) in water to molecular hydrogen (H$_2$), typically with the aid of a sacrificial agent that consumes the concurrently generated holes. First conceptualized in the pioneering work of Fujishima and Honda,[7] this approach offers significant advantages: it utilizes an inexhaustible energy source (sunlight), employs water as the hydrogen source, and operates under ambient conditions.[8,9] The development of highly efficient, stable, and cost-effective semiconductor photocatalysts that can effectively perform this hydrogen evolution reaction (HER) has therefore become a central objective in materials science and renewable energy research.

In the extensive search for suitable HER photocatalysts, strontium titanate (SrTiO$_3$), a perovskite oxide (ABO$_3$), has been established as a benchmark material.[10] Its prominence stems from a combination of favorable properties. Critically, its conduction band minimum (CBM) is sufficiently negative to drive the reduction of protons to H$_2$, providing the necessary thermodynamic potential for the reaction. Furthermore, SrTiO$_3$ exhibits exceptional chemical and photochemical stability in aqueous environments, which is crucial for long-term operational viability.[11] Being composed of earth-abundant, non-toxic elements and accessible *via* cost-effective synthesis, it serves as

[a] Shaanxi Energy Institute, Xianyang 712000, China

[b] The School of Chemistry and Chemical Engineering, Shaanxi University of Science and Technology, Xi'an 710021, China. E-mail: yangyuhao@sust.edu.cn

an excellent platform for designing and investigating advanced materials for solar hydrogen production. Despite these advantages, the practical photocatalytic efficiency of pristine $SrTiO_3$ for hydrogen evolution is severely limited by two fundamental drawbacks. The primary limitation is its wide bandgap of approximately 3.2 eV,[12] which restricts its light absorption to the UV region (∼4–5% of the solar spectrum) and leaves the vast portion of visible light (∼45%) unutilized.[13] The second critical impediment is the rapid recombination of photogenerated electron–hole pairs.[13] Upon photoexcitation, these charge carriers are prone to recombine before electrons can migrate to the surface to participate in the HER, drastically reducing the overall quantum efficiency. Overcoming these limitations is essential to unlock the material's potential for efficient hydrogen evolution.

To overcome these intrinsic deficiencies, numerous modification strategies have been investigated. These strategies aim to either (i) extend the spectral response of $SrTiO_3$ into the visible-light region or (ii) enhance the separation and transport of photogenerated charge carriers, or ideally, achieve both simultaneously. Common approaches include elemental doping (cationic and anionic),[14] surface deposition of noble metal cocatalysts (e.g., Pt, Au) to serve as electron sinks and active sites for H_2 evolution,[15] dye sensitization,[16] and the construction of semiconductor heterojunctions.[17] Among these approaches, fabricating semiconductor heterojunctions has emerged as a particularly effective strategy. A heterojunction formed at the interface of two semiconductors with well-aligned band structures can offer synergistic benefits.[18] First, pairing $SrTiO_3$ with a narrower-bandgap semiconductor can significantly extend the composite's light absorption range into the visible spectrum. Second, the mismatched Fermi levels at the interface often create a built-in electric field, which effectively drives the spatial separation of photogenerated electrons and holes, thereby suppressing their recombination. Various heterojunction configurations, such as type-II, Z-scheme, and the more recently proposed S-scheme, have been designed to optimize charge-carrier dynamics. For example, coupling $SrTiO_3$ with visible-light-responsive materials like Bi_2S_3,[19] has proven effective for enhancing photocatalytic performance. These studies underscore the immense potential of heterojunction engineering for tailoring the optoelectronic properties of $SrTiO_3$-based photocatalysts. Nevertheless, the rational design of multicomponent heterojunctions that can simultaneously optimize broad-spectrum light absorption and establish highly efficient, multistep charge-transfer pathways remains a formidable challenge. Achieving a synergistic interplay between multiple components requires meticulous interfacial engineering and a deep understanding of the underlying charge-carrier dynamics to maximize the yield of photo-electrons for the surface catalytic reaction.

In this study, we address this challenge by designing and synthesizing a novel $SrTiO_3/TiO_2/SrTiS_3$ ternary heterojunction for highly efficient photocatalytic hydrogen evolution. We hypothesize that the strategic integration of these three components will result in synergistic performance enhancement for the HER. The core innovation is the incorporation of

strontium thiotitanate ($SrTiS_3$), which is engineered to fulfill a dual role. First, with its narrower bandgap, $SrTiS_3$ acts as a sensitizer, extending the composite's photoresponse into the visible-light region. Second, and more critically, the engineered band alignment among $SrTiO_3$, TiO_2, and $SrTiS_3$ is designed to create a stepwise charge-transfer cascade. This architecture promotes an efficient, directional migration of photogenerated electrons to the catalyst surface for H_2 production. This suppression of charge recombination and prolongation of carrier lifetime is expected to yield a substantial improvement in the H_2 evolution rate compared to pristine $SrTiO_3$ and its binary counterparts. Herein, we report the synthesis, characterization, and photocatalytic performance of this novel ternary heterojunction and provide compelling evidence for the underlying mechanism responsible for its enhanced activity.

2 Experimental

2.1 Materials

Strontium chloride hexahydrate ($SrCl_2\cdot6H_2O$, analytical reagent), tetrabutyl titanate ($Ti(OBu)_4$, analytical reagent), carbon disulfide (CS_2, analytical reagent), and absolute ethanol (C_2H_5OH, analytical reagent) were purchased from Damao Chemical Reagent Factory (Tianjin, China). Chloroplatinic acid hexahydrate ($H_2PtCl_6\cdot6H_2O$, analytical reagent) was also sourced commercially. All chemicals were used as received without further purification. Deionized (DI) water was prepared in-house using a laboratory purification system.

2.2 Synthesis of $SrTiO_3$

The synthesis of $SrTiO_3$ was carried out via a hydrothermal method. In a typical procedure, 1.58 g of strontium chloride hexahydrate ($SrCl_2\cdot6H_2O$) was dissolved in 20 mL of deionized (DI) water to form solution A. Separately, 3.4 mL of tetrabutyl titanate ($Ti(OBu)_4$) was added to 20 mL of absolute ethanol to form solution B. Subsequently, solution A was added dropwise into solution B under vigorous magnetic stirring. After mixing, 30 mL of a 3 M sodium hydroxide (NaOH) solution was introduced into the mixture. The resulting suspension was stirred continuously for 2 hours at a speed of 500 rpm. The final mixture was then transferred into a 100 mL Teflon-lined stainless-steel autoclave. The autoclave was sealed and maintained at 180 °C for 24 hours in an electric oven. After the reaction, the autoclave was allowed to cool naturally to room temperature. The white precipitate was collected by centrifugation, washed alternately with DI water and absolute ethanol five times to remove any residual ions and impurities, and finally dried in an oven at 80 °C for 8 hours. The resulting white powder was designated as pristine $SrTiO_3$.

2.3 Synthesis of $SrTiO_3/TiO_2/SrTiS_3$ and $SrTiS_3$

The target materials were prepared through a controlled thermal vulcanization of the previously synthesized $SrTiO_3$ powder. The degree of vulcanization was precisely controlled by varying the amount of the sulfur source, carbon disulfide (CS_2). In a typical procedure, 0.1 g of the $SrTiO_3$ powder was loaded

into an alumina boat. A specific volume of CS_2 (ranging from 0.5 mL to 1.0 mL) was then added to the boat, which was immediately transferred into a quartz tube furnace. The system was heated to 800 °C with a heating rate of 5 °C min^{-1} and maintained for 3 hours. The reaction was conducted under the vapor pressure generated by the CS_2. After cooling naturally to room temperature, the resulting powder was collected. By systematically varying the volume of CS_2, a series of composite materials were synthesized. The samples prepared with 0.5, 0.6, 0.7, 0.8, and 0.9 mL of CS_2 were designated as $0.5S/SrTiO_3$, $0.6S/SrTiO_3$, $0.7S/SrTiO_3$, $0.8S/SrTiO_3$, and $0.9S/SrTiO_3$, respectively. These samples are referred to as the $SrTiO_3/TiO_2/SrTiS_3$ ternary composites. During this sulfidation process, partial structural rearrangement and oxygen redistribution occurred, resulting in the *in situ* generation of TiO_2 nanodomains intimately anchored to the $SrTiO_3$ particles. No separate TiO_2 precursor was introduced. The sample prepared with a sufficient excess of CS_2 (1.0 mL) to ensure complete conversion was designated as $1.0S/SrTiO_3$, which corresponds to pristine $SrTiS_3$.

2.4 Characterization

The crystallographic structure and phase purity of the synthesized samples were analyzed by X-ray diffraction (XRD) using a Bruker D8 Advance diffractometer with Cu Kα radiation ($\lambda = 1.5418$ Å). The diffraction patterns were recorded in the 2θ range of 10–80° with a step size of 0.02°. The optical properties of the materials were investigated using a UV-vis diffuse reflectance spectrophotometer (DRS, Shimadzu UV-2600) equipped with an integrating sphere. $BaSO_4$ was used as a reference standard for 100% reflectance. The absorption spectra were converted from the reflectance data using the Kubelka–Munk function. The surface morphology and microstructure of the samples were examined using a field emission scanning electron microscope (FESEM, Hitachi S-8100). Prior to observation, the samples were coated with a thin layer of gold to enhance conductivity. Detailed microstructural analysis, including high-resolution transmission electron microscopy (HRTEM) and selected area electron diffraction (SAED), was performed on a FEI Tecnai G2 F20 S-TWIN transmission electron microscope operating at an acceleration voltage of 200 kV. Samples for TEM analysis were prepared by dispersing the powder in ethanol *via* ultrasonication and dropping the suspension onto a carbon-coated copper grid. The surface elemental composition and chemical valence states were determined by X-ray photoelectron spectroscopy (XPS) on a Thermo Scientific K-Alpha spectrometer with a monochromatic Al Kα X-ray source. All binding energies were calibrated with respect to the adventitious carbon C 1s peak at 284.8 eV. Photoelectrochemical measurements, including transient photocurrent response and electrochemical impedance spectroscopy (EIS), were conducted on a CHI 660E electrochemical workstation (CH Instruments, Shanghai, China) in a standard three-electrode configuration. The working electrode was prepared by dispersing 0.10 g of the photocatalyst powder in 20 mL of anhydrous ethanol, followed by ultrasonic treatment to form a homogeneous suspension. This suspension was drop-cast onto a fluorine-doped tin oxide (FTO) glass substrate and dried under ambient conditions, producing a uniform catalyst film. A platinum foil served as the counter electrode, and a saturated calomel electrode (SCE) was used as the reference electrode. The electrolyte consisted of 0.5 mol per L Na_2SO_4 aqueous solution.

2.5 Photocatalytic hydrogen evolution measurements

The photocatalytic hydrogen evolution activity of the synthesized samples was evaluated in a sealed gas-circulation system connected to a gas chromatograph. In a typical experiment, 20 mg of the photocatalyst powder was dispersed in a solution containing 90 mL of deionized (DI) water and 9 mL of triethanolamine (TEOA, stock solution concentration: 20 vol%) as a sacrificial hole scavenger. It should be noted that "20 vol%" refers to the concentration of the TEOA stock solution itself, rather than its volume fraction in the reaction mixture. To facilitate the *in situ* photodeposition of a platinum cocatalyst, 1.0 mL of an aqueous H_2PtCl_6 solution (0.5 mg mL^{-1}) was added to the suspension, corresponding to approximately 2.5 wt% Pt loading. The resulting suspension was thoroughly sonicated for 15 minutes to ensure a uniform dispersion. The mixture was then transferred to a top-irradiation quartz reaction vessel and stirred continuously at 500 rpm. Prior to irradiation, the entire system was purged with argon for 30 minutes to completely remove dissolved air. The reaction was initiated by irradiating the suspension with a 300 W Xe lamp, which served as a simulated solar light source. At given time intervals every 60 minutes, a 0.5 mL gas sample was automatically extracted from the headspace of the reactor and injected into a gas chromatograph (GC-9790II, Fuli Instruments, China) equipped with a thermal conductivity detector (TCD) and a 5 Å molecular sieve packed column, using high-purity argon as the carrier gas. The amount of H_2 produced was quantified based on a standard calibration curve. All photocatalytic H_2 evolution experiments were conducted at least three times under identical reaction conditions to ensure reproducibility. The H_2 production rates were calculated based on the average of these independent measurements, and the corresponding error bars in Fig. 9b represent the standard deviation (SD) of the data. The deviations were consistently small, indicating the high reproducibility and stability of the experimental setup.

3 Results and discussion

The crystal structure and phase evolution of the synthesized materials were investigated by X-ray diffraction (XRD), with the patterns shown in Fig. 1. The pristine $SrTiO_3$ sample exhibits sharp diffraction peaks at 2θ values of 22.8°, 32.4°, 40.0°, 46.5°, 57.8°, 67.8°, and 77.2°, which can be perfectly indexed to the (100), (110), (111), (200), (211), (220), and (310) crystal planes of the cubic perovskite phase of $SrTiO_3$ (JCPDS no. 74-1296),[19] indicating its high purity and crystallinity. For the samples prepared with low amounts of the sulfur source ($0.5S/SrTiO_3$, $0.6S/SrTiO_3$, and $0.7S/SrTiO_3$), the XRD patterns are nearly identical to that of pristine $SrTiO_3$. This observation suggests that at these lower CS_2 concentrations, the vulcanization
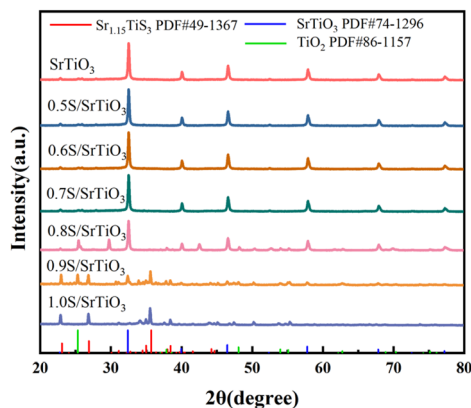
Fig. 1 XRD patterns of prepared samples.

Fig. 2 SEM image of SrTiO$_3$.

reaction is either negligible or confined to the surface region, resulting in changes below the detection limit of XRD. A significant phase transformation is observed for the 0.8S/SrTiO$_3$ sample. While the characteristic peaks of SrTiO$_3$ are still present, their intensity is notably diminished. Concurrently, new diffraction peaks emerge. The peak at 25.3° corresponds to the (101) plane of anatase TiO$_2$ (JCPDS no. 86-1157),[20] and the peaks at 29.7° and 42.4° are attributed to the (200) and (220) planes of SrS (JCPDS no. 08-0489),[21] respectively. The appearance of these new phases signifies the onset of the vulcanization reaction, where SrS and TiO$_2$ are formed as key intermediate products. Upon increasing the CS$_2$ volume to 0.9 mL (0.9S/SrTiO$_3$), the XRD pattern evolves further. The peaks corresponding to the SrS intermediate phase disappear completely. Simultaneously, a new set of peaks appears, which can be indexed to SrTiS$_3$ (JCPDS no. 49-1367).[22] The continued attenuation of the SrTiO$_3$ peaks, alongside the presence of both TiO$_2$ and the newly formed SrTiS$_3$, strongly indicates the successful fabrication of the target SrTiO$_3$/TiO$_2$/SrTiS$_3$ ternary heterostructure. This sample represents an optimal degree of partial vulcanization. Finally, for the 1.0S/SrTiO$_3$ sample prepared with an excess of CS$_2$, the diffraction peaks for both SrTiO$_3$ and TiO$_2$ completely vanish. The pattern exclusively shows the characteristic peaks of the SrTiS$_3$ phase, confirming that the vulcanization reaction has proceeded to completion. In summary, the XRD results provide clear evidence of a controllable, stepwise vulcanization process. The 0.9S/SrTiO$_3$ sample, which clearly contains the three distinct phases of SrTiO$_3$, TiO$_2$, and SrTiS$_3$, was identified as the successfully prepared ternary heterojunction and was therefore selected for subsequent, more detailed characterization and photocatalytic activity evaluation.

The morphology and microstructure of the as-prepared samples were investigated by field emission scanning electron microscopy (SEM), as shown in Fig. 2 and 3. Fig. 2 displays the SEM image well-defined nanocubes with smooth surfaces and an average particle size of approximately 200 nm. This regular cubic morphology is characteristic of hydrothermally synthesized SrTiO$_3$. Fig. 3 presents the SEM images of the S/SrTiO$_3$ series obtained after the thermal vulcanization process with varying amounts of CS$_2$. A clear, progressive evolution in
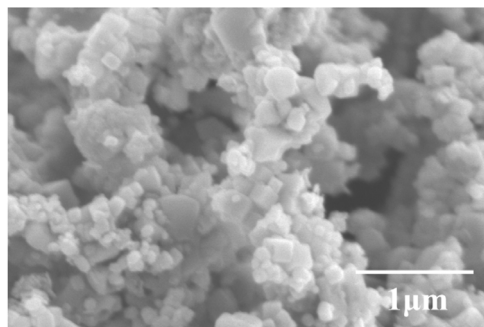
morphology is observed as the CS$_2$ volume increases. For the 0.5S/SrTiO$_3$, 0.6S/SrTiO$_3$, and 0.7S/SrTiO$_3$ samples (Fig. 3a–c), the fundamental cubic shape of the SrTiO$_3$ precursor is largely retained. However, a noticeable increase in particle agglomeration and a slight roughening of the cube surfaces can be seen. This suggests that even at low CS$_2$ concentrations, a surface-level reaction has begun, consistent with the initial stages of vulcanization. These subtle morphological changes occur before significant phase transformations are detectable by XRD, indicating the higher sensitivity of surface morphology to the reaction conditions. As the CS$_2$ volume is increased to 0.8 mL (0.8S/SrTiO$_3$, Fig. 3d), the particle agglomeration becomes more pronounced, and the original cubic structure begins to lose its sharp edges. This morphological shift coincides with the emergence of TiO$_2$ and SrS phases in the XRD pattern, confirming that a more substantial chemical transformation is underway. The morphology of the optimal composite, 0.9S/SrTiO$_3$ (Fig. 3e), is particularly noteworthy. The surface appears significantly rougher and more textured compared to the other samples. This coarsened, heterogeneous surface is indicative of the formation of the SrTiS$_3$ phase alongside the residual SrTiO$_3$ and TiO$_2$ components, as confirmed by XRD. Such a high-surface-area, textured morphology is often beneficial for photocatalysis, as it can provide a greater number of accessible active sites for surface reactions. Finally, upon complete vulcanization to form 1.0S/SrTiO$_3$ (Fig. 3f), the material transforms into larger, irregularly shaped particles with a relatively smoother, more consolidated surface compared to 0.9S/SrTiO$_3$.
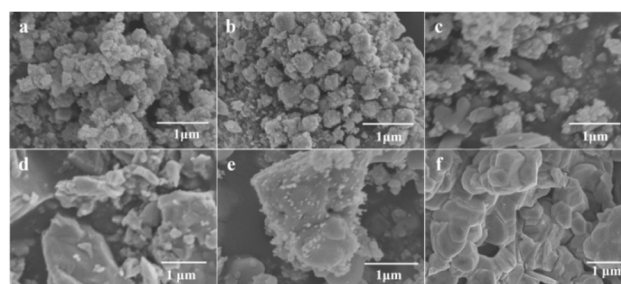

Fig. 3 SEM image of products with different volumes of CS$_2$, (a) 0.5S/SrTiO$_3$, (b) 0.6S/SrTiO$_3$, (c) 0.7S/SrTiO$_3$, (d) 0.8S/SrTiO$_3$, (e) 0.9S/SrTiO$_3$ and (f) 1.0S/SrTiO$_3$.

This change is attributed to the complete conversion to the single-phase SrTiS$_3$ and subsequent crystal growth or sintering at the high reaction temperature. The distinct difference in surface texture between the 0.9S/SrTiO$_3$ composite and the 1.0S/SrTiO$_3$ single phase underscores the unique heterostructured nature of the former.

To further confirm the composition and elemental distribution within the optimal 0.9S/SrTiO$_3$ composite, energy-dispersive X-ray spectroscopy (EDS) mapping was performed, with the results presented in Fig. 4. The mapping images clearly reveal the presence and uniform distribution of all four constituent elements: strontium (Sr), titanium (Ti), oxygen (O), and sulfur (S) throughout the sample's microstructure. The simultaneous detection of both oxygen and sulfur is a crucial finding, providing direct evidence for the coexistence of oxide (SrTiO$_3$, TiO$_2$) and sulfide (SrTiS$_3$) phases within a single particle or agglomerate. This result is in excellent agreement with the XRD analysis (Fig. 1), which identified these three distinct crystalline phases in the 0.9S/SrTiO$_3$ sample. The homogeneous spatial distribution of these elements suggests that the different phases are intimately integrated, which is a prerequisite for the formation of an efficient heterojunction interface. A qualitative comparison of the signal intensities shows that the oxygen signal appears somewhat less intense in relative to the signals for Sr, Ti, and S. This observation suggests that a significant portion of the original SrTiO$_3$ precursor has been converted during the vulcanization process, leaving a smaller fraction of oxide components compared to the newly formed sulfide. This finding aligns with our hypothesis that a further increase in the CS$_2$ supply would lead to the complete conversion of the material into the single-phase SrTiS$_3$, as was observed for the 1.0S/SrTiO$_3$ sample.

To gain deeper insight into the microstructure and verify the formation of the heterojunction at the nanoscale, transmission electron microscopy (TEM) and high-resolution TEM (HRTEM) analyses were performed on the optimal 0.9S/SrTiO$_3$ sample.

Fig. 5a and b show low-magnification TEM images, revealing that the material consists of irregularly shaped nanoparticles with sizes ranging from approximately 50 nm to several hundred nanometers. This morphology, which is an intermediate between granular and lamellar structures, is consistent with the FESEM observations and reflects the structural transformation from the original SrTiO$_3$ nanocubes. The formation of the intimate multi-component heterojunction is
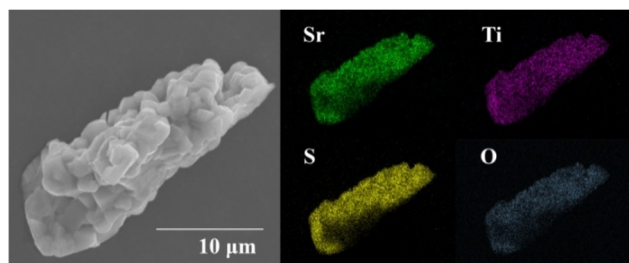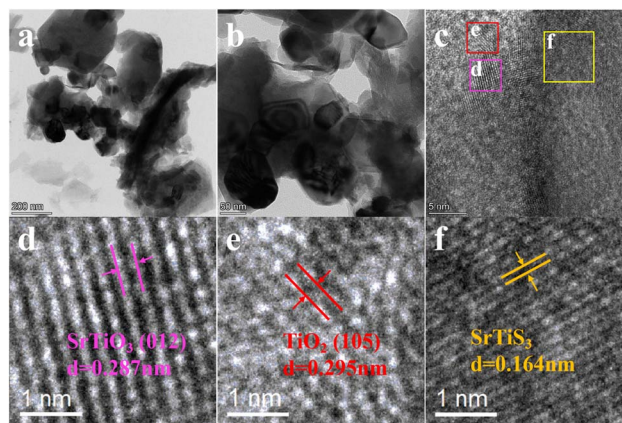

Fig. 5 Transmission electron microscopy (TEM) (a and b) and high-resolution TEM (HRTEM) (c–f) image of 0.9S/SrTiO$_3$ sample.

unequivocally confirmed by the HRTEM analysis. Fig. 5c presents a high-resolution image of a selected interfacial region, where distinct domains with different lattice fringe patterns are clearly visible in close proximity.

To identify these phases, specific areas within this region were further magnified, as shown in Fig. 5d–f. In Fig. 5d, clear and well-defined lattice fringes with an interplanar spacing of 0.287 nm are measured, which corresponds perfectly to the (012) crystal plane of cubic SrTiO$_3$. Adjacent to this region, as shown in Fig. 5e, a different set of lattice fringes with a spacing of 0.295 nm is observed, which can be indexed to the (105) plane of anatase TiO$_2$. Finally, Fig. 5f highlights a third distinct domain exhibiting a lattice spacing of 0.164 nm, which is characteristic of the plane of SrTiS$_3$. The clear observation of these three distinct, well-resolved lattice fringes corresponding to SrTiO$_3$, TiO$_2$, and SrTiS$_3$ within a single nanostructure provides direct and compelling evidence for the successful synthesis of the SrTiO$_3$/TiO$_2$/SrTiS$_3$ ternary heterojunction. The intimate contact between these phases at the atomic level is expected to facilitate efficient charge carrier separation and transfer, which is critical for enhanced photocatalytic activity.

The light-harvesting capabilities of the as-prepared photocatalysts were investigated by UV-vis diffuse reflectance spectroscopy (DRS), and the results are presented in Fig. 6. Fig. 6
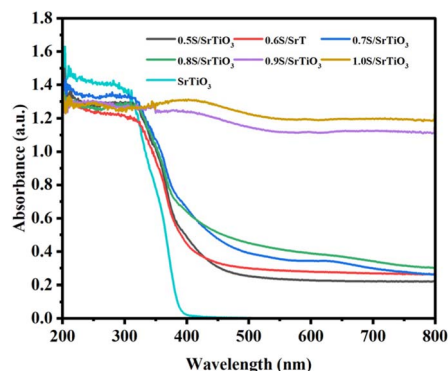

Fig. 4 Energy-dispersive X-ray spectroscopy (EDS) mapping of 0.9S/SrTiO$_3$.

Fig. 6 UV-vis diffuse reflectance spectroscopy (DRS) of samples.

displays the UV-vis absorption spectra of pristine $SrTiO_3$ and the $S/SrTiO_3$ series. The pristine $SrTiO_3$ sample exhibits a sharp absorption edge located in the ultraviolet region at approximately 390 nm, consistent with its wide band gap nature. Consequently, its ability to absorb visible light is negligible. In stark contrast, all vulcanized samples show a significant red-shift in their absorption edges, extending well into the visible light region and even into the near-infrared (NIR) region. This broadened spectral response is a direct consequence of the incorporation of sulfur and the formation of the narrower-band-gap $SrTiS_3$ phase. As the volume of CS_2 used in the synthesis increases from 0.5 mL to 1.0 mL, the absorption edge progressively shifts to longer wavelengths, and the overall absorption intensity across the visible spectrum is enhanced. Notably, the $0.9S/SrTiO_3$ and $1.0S/SrTiO_3$ samples demonstrate strong, broad-spectrum absorption, indicating their superior light-harvesting efficiency compared to pristine $SrTiO_3$ and the composites with lower sulfur content. This enhanced light absorption is crucial for generating a larger number of photogenerated charge carriers under solar irradiation. The band gap energy (E_g) for each sample was estimated from the Tauc plots derived from the DRS data.[23] The pristine $SrTiO_3$ has a calculated band gap of 3.20 eV. Upon vulcanization, the band gap of the composites systematically decreases with the increasing amount of CS_2. This trend corroborates the XRD results, confirming that a higher degree of vulcanization leads to a greater proportion of the narrow-band-gap $SrTiS_3$ phase in the composites. A significant reduction in the band gap is observed for the $0.8S/SrTiO_3$ (2.74 eV) and $0.9S/SrTiO_3$ (2.38 eV) samples, which marks the critical point where substantial phase transformation occurs. The band gap of the fully vulcanized $1.0S/SrTiO_3$ (pristine $SrTiS_3$) was determined to be 2.35 eV. While the significantly narrowed band gap of the composites is highly beneficial for capturing more solar energy, an excessively narrow band gap can sometimes be detrimental. If the band edge potentials are not well-aligned for the redox reactions, or if the driving force for charge separation is reduced, it could potentially increase the recombination rate of photogenerated electron–hole pairs. Therefore, an optimal balance between light absorption and charge separation efficiency is essential, which is a key motivation for designing the heterostructure.

To probe the efficiency of photogenerated charge carrier separation and transfer, which are critical factors governing photocatalytic activity, photoelectrochemical measurements were conducted. The transient photocurrent responses and electrochemical impedance spectra (EIS) of the as-prepared samples are presented in Fig. 7. Fig. 7a displays the transient photocurrent (I–t) curves recorded under intermittent light irradiation. The pristine $SrTiO_3$ sample exhibits a very weak photocurrent density, which is consistent with its poor visible light absorption and high rate of electron–hole recombination. In contrast, all vulcanized samples show a significantly enhanced photocurrent response. The photocurrent density generates a larger population of charge carriers, and (ii) the well-formed $SrTiO_3/TiO_2/SrTiS_3$ heterojunction interface (i) the broadened light absorption (as confirmed by UV-vis DRS)
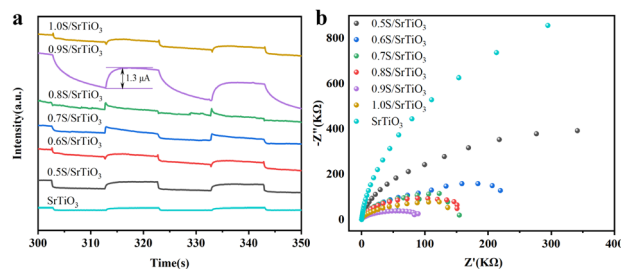

Fig. 7 The transient photocurrent responses (a) and electrochemical impedance spectra (EIS) (b) of the as-prepared samples.

effectively promotes the spatial separation of these charge carriers, suppressing their recombination and allowing more electrons to contribute to the photocurrent. However, when the CS_2 volume was increased to 1.0 mL (forming pure $SrTiS_3$), the photocurrent density decreased. This decline, despite the sample's excellent light absorption, suggests that the absence of the heterojunction leads to a higher rate of charge recombination, underscoring the critical role of the heterostructure in facilitating efficient charge separation.

Further evidence for the enhanced charge transfer kinetics is provided by the EIS Nyquist plots, shown in Fig. 7b. The radius of the semicircle in a Nyquist plot is typically associated with the charge transfer resistance at the electrode/electrolyte interface; a smaller radius implies a lower resistance and more efficient charge transfer. The pristine $SrTiO_3$ exhibits the largest semicircle, indicating a very high charge transfer resistance. Following vulcanization, all S-containing samples display significantly smaller semicircles, confirming that the formation of the sulfide phase facilitates more efficient interfacial charge transfer. Consistent with the photocurrent results, the arc radius progressively decreases with increasing CS_2 content up to 0.9 mL. The $0.9S/SrTiO_3$ sample exhibits the smallest semicircle, signifying the lowest charge transfer resistance. This result strongly supports the conclusion that the ternary heterojunction provides the most effective pathways for separating charge carriers and transferring them to the electrolyte. The slight increase in the arc radius for the $1.0S/SrTiO_3$ sample again points to less efficient charge separation in the single-phase material compared to the optimized heterojunction. It should be noted that the photocurrent and EIS analyses are inherently different in mechanism and time-scale sensitivity, and several previous studies have also reported that their relative trends may not be exactly the same. Even so, both techniques in our work consistently indicate that the $SrTiO_3/TiO_2/SrTiS_3$ heterojunction provides the most efficient charge separation and rapid interfacial electron transfer among all tested samples.

In summary, both the transient photocurrent and EIS results consistently demonstrate that the $0.9S/SrTiO_3$ ternary heterojunction possesses superior charge separation and transfer efficiency. This is a direct consequence of the synergistic interplay between enhanced visible light absorption and the effective charge-driving force provided by the engineered heterostructure.
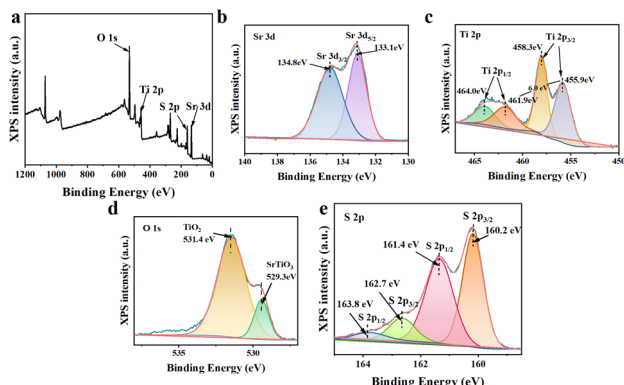
Fig. 8 X-ray photoelectron spectroscopy (XPS) patterns of as-prepared samples.

To elucidate the surface elemental composition and chemical valence states of the optimal $0.9S/SrTiO_3$ composite, X-ray photoelectron spectroscopy (XPS) was performed. Fig. 8a presents the XPS survey spectrum, which clearly confirms the presence of Sr, Ti, O, and S on the surface of the sample, consistent with the bulk composition determined by XRD and EDS analysis. High-resolution spectra for each element were then collected to identify their specific chemical states. The high-resolution spectrum of Sr 3d, shown in Fig. 8b, can be deconvoluted into two peaks at binding energies of 133.1 eV and 134.8 eV, corresponding to the $Sr\ 3d_{5/2}$ and $Sr\ 3d_{3/2}$ spin–orbit doublet, respectively. These peaks are characteristic of Sr^{2+} ions in the perovskite lattice of $SrTiO_3$.[24] A slight positive shift of 0.1 eV in these binding energies is observed compared to pristine $SrTiO_3$. This shift suggests a decrease in the electron cloud density around the Sr^{2+} ions, which can be attributed to the strong electronegativity of neighboring sulfur atoms and the electronic interactions at the heterojunction interface. The Ti 2p high-resolution spectrum in Fig. 8c provides compelling evidence for the coexistence of different titanium species. The spectrum can be fitted with two distinct spin–orbit doublets. The first doublet, with peaks at 458.3 eV ($Ti\ 2p_{3/2}$) and 464.0 eV ($Ti\ 2p_{1/2}$), exhibits a spin–orbit splitting of 5.7 eV, which is characteristic of Ti^{4+} in the $SrTiO_3$ lattice.[24] The second doublet, located at lower binding energies of 455.9 eV ($Ti\ 2p_{3/2}$) and 461.9 eV ($Ti\ 2p_{1/2}$), has a splitting of 6.0 eV and is assigned to Ti^{4+} in the $SrTiS_3$ environment. The presence of both Ti^{4+} states unequivocally confirms the coexistence of $SrTiO_3$ and $SrTiS_3$ on the catalyst's surface. The O 1s spectrum, displayed in Fig. 8d, can be deconvoluted into two main components. The dominant peak at 529.3 eV is assigned to the lattice oxygen (O^{2-}) in the Sr–O–Ti bonds of the $SrTiO_3$ structure. The second, slightly higher binding energy peak at 531.4 eV corresponds to the lattice oxygen in the Ti–O bonds of the TiO_2 phase. This finding confirms the presence of the TiO_2 component in the ternary composite, in excellent agreement with the XRD results. Finally, the high-resolution S 2p spectrum (Fig. 8e) reveals the chemical state of sulfur. The spectrum shows a characteristic doublet corresponding to $S\ 2p_{3/2}$ and $S\ 2p_{1/2}$. The binding energies of these peaks fall within the typical range for metal sulfides (160–

164 eV), confirming that sulfur exists in the S^{2-} (sulfide) state within the $SrTiS_3$ lattice, rather than in higher oxidation states such as sulfite or sulfate. To further verify the successful formation of the $SrTiO_3/TiO_2/SrTiS_3$ heterojunction, XPS analysis was performed for both the pure $SrTiO_3$ and the ternary composite $0.9S/SrTiO_3$. As shown in Fig. S1 (SI), the binding energies of Sr 3d, Ti 2p, S 2p, and O 1s peaks in the composite exhibit distinct shifts relative to those in pure $SrTiO_3$. Specifically, the Sr 3d peaks shift toward higher binding energies. Such binding energy changes are commonly associated with electronic interaction across the heterojunction, confirming the intimate contact and effective charge transfer pathways constructed in the $SrTiO_3/TiO_2/SrTiS_3$ system.

In summary, the detailed XPS analysis provides definitive evidence for the surface composition of the $0.9S/SrTiO_3$ composite, confirming the simultaneous presence of $SrTiO_3$, TiO_2, and $SrTiS_3$. Furthermore, the observed shifts in binding energies suggest strong electronic coupling between these components, which is fundamental to the formation of an efficient heterojunction for charge separation.

The photocatalytic H_2 evolution activity of the as-prepared samples was evaluated under simulated solar light irradiation using triethanolamine (TEOA) as a sacrificial agent. Fig. 9a presents the total amount of H_2 produced over a 6 hour period for pristine $SrTiO_3$ and the $S/SrTiO_3$ series. The pristine $SrTiO_3$ exhibited only minimal H_2 evolution, which is consistent with its limited light absorption and poor charge separation efficiency. Upon vulcanization, all $S/SrTiO_3$ samples demonstrated significantly improved photocatalytic performance. A clear trend was observed: the H_2 production increased systematically as the CS_2 volume used in synthesis was raised from 0.5 mL to 0.9 mL. This enhancement is attributed to the narrowed band gap of the composites, which improves visible light harvesting, as confirmed by the UV-vis spectra.[25] The $0.9S/SrTiO_3$ composite achieved the highest total H_2 yield, indicating its superior catalytic activity. However, a sharp decline in H_2 production was observed for the $1.0S/SrTiO_3$ sample (pure $SrTiS_3$), despite its excellent light absorption capabilities. This critical result highlights that enhanced light absorption alone is insufficient for high activity; efficient charge separation is equally important. To quantitatively compare the performance, the average H_2 evolution rates were calculated and are presented in Fig. 9b. The pristine $SrTiO_3$ sample yielded a modest rate of 7.5 μmol $g^{-1}\ h^{-1}$. The rate progressively increased with the degree of vulcanization, reaching a maximum for the $0.9S/SrTiO_3$ composite, which delivered an impressive average H_2 evolution rate of 85.5 μmol $g^{-1}\ h^{-1}$. This represents an 11.4-fold enhancement compared to pristine $SrTiO_3$. The superior performance of the $0.9S/SrTiO_3$ sample is a direct result of the synergistic effects of the $SrTiO_3/TiO_2/SrTiS_3$ ternary heterojunction. Furthermore, the apparent quantum yield (AQY) at 420 nm was determined to be 8.9% (calculation details in SI), which is among the higher values reported for similar oxide/sulfide heterojunction photocatalysts. This further validates the superior photocatalytic activity of the $SrTiO_3/TiO_2/SrTiS_3$ system compared to literature benchmarks under comparable testing conditions. The $SrTiS_3$ component acts as a sensitizer to
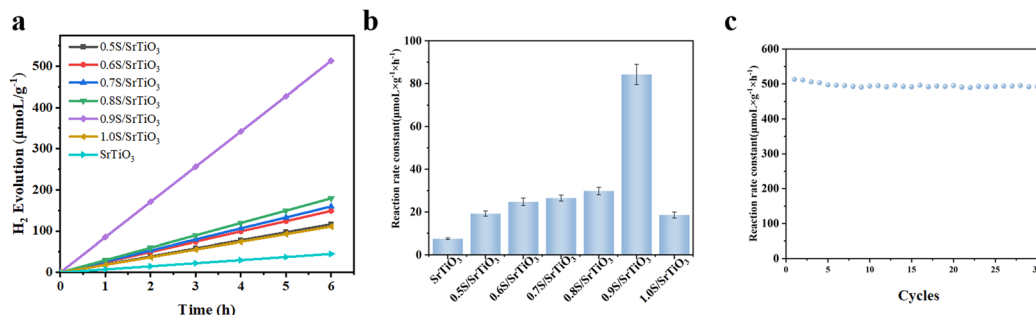
Fig. 9 The photocatalytic H_2 evolution activity (a and b) and the stable tests (c) of the as-prepared samples.

broaden light absorption, while the engineered band alignment at the multiple interfaces promotes efficient separation of photogenerated electron–hole pairs, as evidenced by the photoelectrochemical measurements. The subsequent drop in activity for the 1.0S/SrTiO$_3$ sample (18.5 μmol g^{-1} h^{-1}) confirms that without the beneficial charge separation effect of the heterojunction, severe recombination of charge carriers occurs, leading to diminished catalytic performance.

To further evaluate the long-term durability of the SrTiO$_3$/TiO$_2$/SrTiS$_3$ heterojunction photocatalyst for practical applications, extended photocatalytic H$_2$ evolution tests were performed under continuous irradiation. The optimized 0.9S/SrTiO$_3$ sample cycles every 6 hours, and it has completed 30 cycles in total of uninterrupted operation, and the amount of evolved H$_2$ was recorded at regular intervals. As shown in Fig. 9c, the catalyst maintained ∼96% of its initial activity after 30 cycles, indicating only a slight decrease in performance. This excellent durability can be attributed to the robust structural integrity of the heterojunction and the strong interfacial contact among SrTiO$_3$, TiO$_2$, and SrTiS$_3$, which minimize photocorrosion and preserve the charge transfer pathways over prolonged operation. These results confirm that the ternary heterojunction not only exhibits high initial activity but also possesses the stability required for sustained solar hydrogen production.

To determine the band edge positions of the key semiconductor components and to construct a plausible charge transfer mechanism for the heterojunction, Mott–Schottky

measurements were performed.[26–28] Based on the XRD results, which confirmed that the 1.0S/SrTiO$_3$ sample consists of pure SrTiS$_3$, we used this sample to represent the SrTiS$_3$ component. The Mott–Schottky plots for pristine SrTiO$_3$ and 1.0S/SrTiO$_3$ (SrTiS$_3$) are presented in Fig. 10. Both samples exhibit a positive slope in their respective linear regions ($1/C^2$ vs. E), which is a characteristic feature of n-type semiconductors. This indicates that the introduction of sulfur and the formation of SrTiS$_3$ did not alter the n-type conductivity inherent to the SrTiO$_3$ precursor. For an n-type semiconductor, the flat-band potential (E_{fb}) can be determined by extrapolating the linear portion of the plot to the x-axis (where $1/C^2 = 0$). As shown in Fig. 10a, the E_{fb} of pristine SrTiO$_3$ was determined to be −0.46 V vs. Ag/AgCl. The conduction band minimum (CBM) of an n-type semiconductor is typically located approximately 0.2 eV more negative than its E_{fb}. Therefore, the CBM of SrTiO$_3$ is estimated to be −0.66 V vs. Ag/AgCl. Using the band gap energy (E_g = 3.20 eV) obtained from the Tauc plot (Fig. 6b), the valence band maximum (VBM) was calculated using the equation $E_{VBM} = E_{CBM} + E_g$. The VBM of SrTiO$_3$ was thus determined to be 2.54 V vs. Ag/AgCl. Similarly, the E_{fb} of the SrTiS$_3$ sample was determined to be −0.19 V vs. Ag/AgCl from its Mott–Schottky plot (Fig. 10). This yields a CBM position of −0.39 V vs. Ag/AgCl. With its band gap of 2.35 eV, the VBM of SrTiS$_3$ was calculated to be 1.96 V vs. Ag/AgCl. The determination of these band edge potentials is crucial for understanding the electronic landscape of the SrTiO$_3$/TiO$_2$/SrTiS$_3$ composite. The relative alignment of the conduction and valence bands of each component dictates the pathway for photogenerated charge carrier migration, which will be discussed in the following section.

Based on the comprehensive experimental and theoretical analysis, a multi-step charge separation mechanism across the dual heterojunction interfaces is proposed to account for the superior photocatalytic H$_2$ evolution of the 0.9S/SrTiO$_3$ ternary composite. This mechanism, schematically illustrated in Fig. 11, relies on the specific band alignment of SrTiO$_3$ (CBM/VBM: −0.66/2.54 V), TiO$_2$ (−0.62/2.63 V), and SrTiS$_3$ (−0.39/1.96 V). Upon irradiation with simulated solar light, electron–hole pairs are generated in all three semiconductor components. The unique band structure then orchestrates a highly efficient, directional flow of charge carriers: (1) cascaded electron transfer pathway: a clear potential gradient exists for the
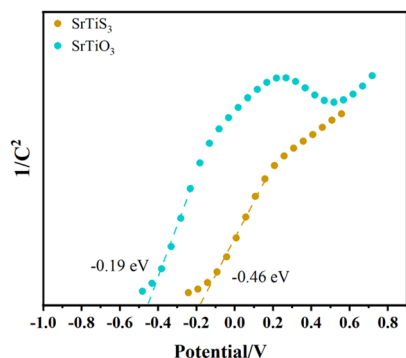

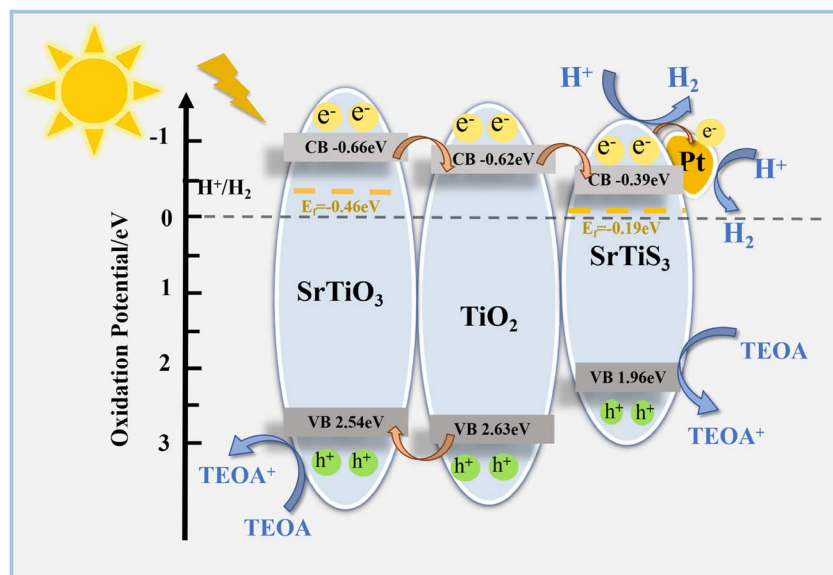**Fig. 10** The Mott–Schottky plots for pristine SrTiO$_3$ and 1.0S/SrTiO$_3$ (SrTiS$_3$).

Fig. 11 Mechanism for the enhanced photocatalytic H_2 evolution over the 0.9S/SrTiO$_3$ ternary heterojunction.

photogenerated electrons. Electrons from the CB of SrTiO$_3$ (−0.66 V) migrate to the more positive CB of TiO$_2$ (−0.62 V). Subsequently, these electrons, along with those generated in TiO$_2$, continue their "downhill" migration to the CB of SrTiS$_3$ (−0.39 V). This cascaded pathway effectively funnels and accumulates the photogenerated electrons onto the SrTiS$_3$ component. These electrons are then transferred to the deposited Pt cocatalyst particles, which act as active sites for the reduction of H^+ to H_2; (2) selective hole migration and confinement: the hole migration pathway is distinctly different and non-linear. The VBM potentials of TiO$_2$ (2.63 V) and SrTiO$_3$ (2.54 V) are very close, allowing for efficient hole transfer from TiO$_2$ to SrTiO$_3$. However, the large potential difference between the VBM of TiO$_2$ (2.63 V) and SrTiS$_3$ (1.96 V) creates a significant energy barrier, effectively inhibiting hole migration from TiO$_2$ to SrTiS$_3$. As a result, the photogenerated holes are primarily confined to the SrTiO$_3$ and TiO$_2$ components; (3) overall charge separation and reaction sites: this sophisticated mechanism achieves a highly effective spatial separation of charge carriers. Electrons are ultimately enriched on the Pt/SrTiS$_3$ side, serving as the reduction sites for H_2 evolution. Holes are localized on the SrTiO$_3$/TiO$_2$ side, which become the oxidation sites. The sacrificial agent, triethanolamine (TEOA), then effectively scavenges these localized holes on both the SrTiO$_3$ and SrTiS$_3$ surfaces, preventing charge recombination and completing the photocatalytic cycle.

This proposed multi-step separation model perfectly explains the experimental observations. It leverages the SrTiS$_3$ as a visible-light sensitizer and the ultimate electron collector, while the SrTiO$_3$/TiO$_2$ heterostructure acts as an efficient hole confinement unit. The synergistic interplay between these components drastically suppresses charge recombination, as evidenced by the enhanced photocurrent and reduced impedance. The absence of this engineered charge separation architecture in the single-phase 1.0S/SrTiO$_3$ explains its inferior

performance, thereby validating the rational design of the ternary heterojunction.

In addition to the enhanced photocatalytic activity and charge separation mechanism, the one-step thermal vulcanization strategy presented here possesses inherent advantages for practical scale-up. The method employs inexpensive, readily available precursors, moderate reaction temperatures, and a straightforward apparatus, which collectively facilitate transition from gram-scale laboratory synthesis to larger batch or even continuous production. Potential challenges during scale-up, such as ensuring uniform heating and safely handling sulfur-containing off-gases, can be addressed with established chemical engineering solutions. Conceptually, this synthetic route can be extended to a variety of oxide/sulfide heterojunctions by selecting appropriate oxide precursors (*e.g.*, ZnO, BiVO$_4$, Nb$_2$O$_5$) and tuning the reaction conditions to tailor the resulting band structures for specific photocatalytic targets. Such scalability and versatility underscore the generality of this approach and its potential to serve as a universal platform for developing advanced photocatalysts for solar energy conversion and related applications.

4 Conclusions

In summary, a novel SrTiO$_3$/TiO$_2$/SrTiS$_3$ ternary heterojunction photocatalyst was successfully designed and synthesized *via* a controlled, one-step thermal vulcanization method. The systematic investigation revealed that the sample prepared with 0.9 mL of CS$_2$ (0.9S/SrTiO$_3$) exhibited the optimal composition and structure. Comprehensive characterization using XRD, SEM, TEM, and XPS confirmed the successful formation of an intimate three-component heterostructure, where SrTiO$_3$, anatase TiO$_2$, and SrTiS$_3$ phases coexist. The incorporation of the narrow-band-gap SrTiS$_3$ component significantly broadened the light absorption range of the composite into the visible and

even near-infrared regions, a stark improvement over pristine SrTiO$_3$. More importantly, the engineered ternary heterostructure demonstrated vastly superior charge separation and transfer efficiency, as evidenced by enhanced photocurrent responses and significantly reduced charge transfer resistance in photo-electrochemical tests. Consequently, the optimized 0.9S/SrTiO$_3$ composite delivered a remarkable photocatalytic H$_2$ evolution rate of 85.5 μmol g^{-1} h^{-1}, which is 11.4 times higher than that of pristine SrTiO$_3$. This outstanding performance is attributed to a multi-step charge separation mechanism across the dual type-II interfaces. In this mechanism, photogenerated electrons are efficiently funneled through a cascaded pathway to the SrTiS$_3$ component, while holes are effectively confined to the SrTiO$_3$/TiO$_2$ side. This spatial separation drastically minimizes charge recombination and maximizes the availability of electrons for the hydrogen evolution reaction. Furthermore, the composite exhibited excellent stability over five consecutive cycles. This work not only presents a highly efficient photocatalyst for solar hydrogen production but also provides a clear example of how rational heterojunction engineering can overcome the intrinsic limitations of wide-band-gap semiconductors. The findings underscore the potential of designing multi-component sulfide/oxide composites as a promising strategy for developing advanced materials for solar energy conversion and other photocatalytic applications.

Author contributions

Chan Lu: conceptualization, investigation, formal analysis, writing – original draft; Xiaolong Li: investigation, methodology, funding acquisition; Yongning Ma: investigation, resources, funding acquisition; Yuhao Yang: conceptualization, supervision, project administration, writing – review & editing.

Conflicts of interest

There are no conflicts to declare.

Data availability

All data included in this study are available upon request by contact with the corresponding author.

Supplementary information is available. See DOI: https://doi.org/10.1039/d5ra05569e.

Acknowledgements

References

1 Q. Chen, H. Zhang, Y.-Y. Lau, T. Wang, W. Wang and G. Zhang, *Sustainability*, 2023, **15**, 5723.

2 M. Child and C. Breyer, *Energy Policy*, 2017, **107**, 11–26.

3 Q. Jia, T. Zhang, Z. Zhu, R. Cai, K. Song, F. Yan and A. Qayyum, *Int. J. Hydrogen Energy*, 2025, **118**, 93–101.

4 J. Huang, B. Hu, J. Meng, T. Meng, W. Liu, Y. Guan, L. Jin and X. Zhang, *Energy Environ. Sci.*, 2024, **17**, 1007–1045.

5 H. Nishiyama, T. Yamada, M. Nakabayashi, Y. Maehara, M. Yamaguchi, Y. Kuromiya, Y. Nagatsuma, H. Tokudome, S. Akiyama, T. Watanabe, R. Narushima, S. Okunaka, N. Shibata, T. Takata, T. Hisatomi and K. Domen, *Nature*, 2021, **598**, 304–307.

6 S. Guo, X. Li, J. Li and B. Wei, *Nat. Commun.*, 2021, **12**, 1343.

7 A. Fujishima and K. Honda, *Nature*, 1972, **238**, 37–38.

8 M. Rafique, R. Mubashar, M. Irshad, S. S. A. Gillani, M. B. Tahir, N. R. Khalid, A. Yasmin and M. A. Shehzad, *J. Inorg. Organomet. Polym. Mater.*, 2020, **30**, 3837–3861.

9 F. Xu and B. Weng, *J. Mater. Chem. A*, 2023, **11**, 4473–4486.

10 M. S. Alshammari, W. H. Hassan, M. M. Al-Zahiwat, H. Osman, H. A. El-Sabban, M. A. Diab, Z. Atamuratova, E. Saitov and A. Amari, *FlatChem*, 2025, **50**, 100841.

11 H. Ma, W. Yang, H. Tang, Y. Pan, W. Li, R. Fang, Y. Shen and F. Dong, *J. Hazard. Mater.*, 2023, **452**, 131269.

12 M. Ahmadi, M. S. Dorraji, M. H. Rasoulifard and A. R. Amani-Ghadim, *Sep. Purif. Technol.*, 2019, **228**, 115771.

13 Z. Jiao, T. Chen, J. Xiong, T. Wang, G. Lu, J. Ye and Y. Bi, *Sci. Rep.*, 2013, **3**, 2720.

14 Y. Xu, Y. Liang, Q. He, R. Xu, D. Chen, X. Xu and H. Hu, *Bull. Mater. Sci.*, 2022, **46**, 6.

15 X. Zhou, N. Liu, T. Yokosawa, A. Osvet, M. E. Miehlich, K. Meyer, E. Spiecker and P. Schmuki, *ACS Appl. Mater. Interfaces*, 2018, **10**, 29532–29542.

16 K. Han, W. Li, C. Ren, H. Li, X. Liu, X. Li, X. Ma, H. Liu and A. Khan, *J. Taiwan Inst. Chem. Eng.*, 2020, **112**, 4–14.

17 M. Ganapathy, Y. Hsu, J. Thomas, L.-Y. Chen, C.-T. Chang and V. Alagan, *Energy Fuels*, 2021, **35**, 14995–15004.

18 C.-E. Tan, J.-T. Lee, E.-C. Su and M.-Y. Wey, *Int. J. Hydrogen Energy*, 2020, **45**, 13330–13339.

19 Y.-T. Lin, Y.-H. Wang, J. C. Wu and X. Wang, *Appl. Catal., B*, 2021, **281**, 119517.

20 P. Londhe, N. B. Chaure and A. Athawale, *Mater. Today Commun.*, 2021, **29**, 102924.

21 S. Shao, K. Du, K. Huang, L. Cheng, X. Mi, P. Zhou, H. Lin, S. Cui, T. Lin, Z. Ba and X. Zhang, *Adv. Powder Technol.*, 2014, **25**, 1516–1519.

22 J. H. Al Shuhaib, J. F. Fernández, J. Bodega, J. R. Ares, I. J. Ferrer and F. Leardini, *Mater. Res. Bull.*, 2023, **167**, 112405.

23 M. K. Guediri, D. Chebli, A. Bouguettoucha, R. Bourzami and A. Amrane, *Environ. Sci. Pollut. Res.*, 2022, **29**, 28098–28114.

24 P. F. Lim, K. H. Leong, L. C. Sim, W.-D. Oh, Y. H. Chin, P. Saravanan and C. Dai, *Appl. Phys. A:Mater. Sci. Process.*, 2020, **126**, 550.

25 K. V. Y. Jie, M. F. Ahmad, A. R. Mohmad, A. M. Ismail, M. N. Norizan, M. M. Ramli, S. Shaari, Y. Sulaiman, S. A. A. Rais and S. Johari, *ACS Appl. Energy Mater.*, 2024, **7**, 799–809.

26 Y.-Y. Sun, M. L. Agiorgousis, P. Zhang and S. Zhang, *Nano Lett.*, 2015, **15**, 581–585.

27 B. L. Phoon, C. W. Lai, J. C. Juan, P. Show and W. Chen, *Int. J. Energy Res.*, 2019, **43**, 5151–5174.

28 Y. Wei, J. Wang, R. Yu, J. Wan and D. Wang, *Angew. Chem., Int. Ed.*, 2019, **58**, 1422–1426.